Nanoscale Advances

ROYAL SOCIETY OF CHEMISTRY

PAPER

View Article Online
View Journal | View Issue

Cite this: *Nanoscale Adv.*, 2025, **7**, 7306

Carbon–polyaniline coaxial structures for enhanced charge transfer and capacitance in supercapacitors

Pham Thi Thuy Nga,[a] Nguyen Van Quy,[a] Dinh Khoi Dang,[a] Nguyen Thanh Sang,[a] Ho Phuong,[a] Nguyen Tran Nhac Khoa,[bc] To Minh Dai.,[bc] Huynh Le Thanh Nguyen *[bc] and Ly Tan Nhiem *[a]

Polyaniline (PANI) is widely used as a pseudocapacitive material in supercapacitors. However, PANI exhibits limited capacitance due to its poor electrical conductivity and low specific surface area. In this study, coaxial structures composed of silver nanowires (AgNWs) as the core, subsequently deposited with a carbon layer and PANI nanowires *via in situ* polymerization, were fabricated. Scanning electron microscopy revealed that the structures had an average diameter of 181 ± 57 nm and a length of 1.2 ± 0.6 μm. X-ray photoelectron spectroscopy analysis verified the successful formation of PANI on the outer layer of the structures, with fully benzenoid units and protonated amines. Raman spectra confirmed the deposition of sp^2-hybridized carbon layers on the AgNW cores. Electrochemical impedance spectroscopy and galvanostatic charge–discharge (GCD) measurements revealed an improved charge transfer resistance (R_{ct}) of 1.43 Ω and a specific capacitance of 184 F g^{-1}, respectively, highlighting the role of the carbon layer in enhancing R_{ct}. After 3000 charge–discharge cycles using a Swagelok model, a capacitance loss of 47% was observed. Cyclic voltammetry measurements, combined with the Dunn method, indicated that the coaxial structures exhibited both electric double-layer capacitance (EDLC), contributing 69%, and pseudocapacitance from redox reactions in PANI. In addition, the coaxial structure was successfully deposited on a flexible ITO-coated PET substrate and subjected to 3000 GCD cycles. The fabricated AgNWs–carbon–PANI coaxial structures exhibited superior charge-storage performance compared to bulk PANI, underscoring their potential for practical energy storage applications in flexible devices.

Received 24th April 2025
Accepted 11th September 2025

DOI: 10.1039/d5na00402k

rsc.li/nanoscale-advances

Introduction

Polyaniline (PANI) is a conducting polymer that has been extensively studied for energy storage applications.[1,2] PANI exhibits intrinsic electrical conductivity in its emeraldine salt (ES) form, which results from protonation using strong acids such as H_2SO_4, enabling excellent electrochemical characteristics as an effective pseudocapacitive material.[3,4] Unlike conventional carbon-based materials that store charge solely through electric double-layer capacitance (EDLC), PANI provides additional capacitance through faradaic redox reactions.[2,3] Specifically, the ES form undergoes reversible redox transitions, forming leucoemeraldine salt and/or pernigraniline salt, thereby facilitating electrical charge storage. However, the pseudocapacitive behavior of PANI is primarily surface-dominated, with only a few nanometers of the material actively participating in redox reactions.[5,6] Consequently, bulk PANI exhibits limited capacitance due to its low specific surface area, which restricts electrolyte ion accessibility.[7] Since supercapacitors rely on rapid charge transfer at the electrode/electrolyte interface, the low electrical conductivity of bulk PANI, as a semiconducting polymer, further limits electron transport, resulting in slower charge and discharge rates.[8] This drawback is particularly problematic in high-power applications, such as hybrid electric vehicles or high-frequency electronics, where rapid charge/discharge cycles are essential.[9,10] To overcome these challenges, the incorporation of PANI with nanostructured materials is a promising strategy.[11,12] Silver nanowires (AgNWs), one-dimensional nanostructures composed of silver atoms, have emerged as excellent candidates.[13,14] AgNWs have gained significant attention in applications such as flexible electronics,[15] sensors,[16] and antimicrobial coatings,[17] due to their unique electrical, optical, and mechanical properties. These properties include exceptionally high electrical conductivity (6.3×10^7 S m^{-1}), high optical transmittance (85–90%), and mechanical flexibility, allowing them to withstand bending, stretching, and twisting without significant

[a]*Faculty of Chemical and Food Technology, Ho Chi Minh City University of Technology and Education, 01 Vo Van Ngan Street, Thu Duc Ward, Ho Chi Minh City, Vietnam*
[b]*Faculty of Chemistry, University of Science, 227 Nguyen Van Cu Street, Cho Quan Ward, Ho Chi Minh City, Vietnam*
[c]*Vietnam National University Ho Chi Minh City (VNU-HCM), Dong Hoa Ward, Ho Chi Minh City, Vietnam*

loss of conductivity.[13,18] Notably, AgNWs stabilized by polyvinylpyrrolidone (PVP) exhibit strong binding affinity to silver surfaces due to lone-pair interactions between oxygen/nitrogen atoms in PVP and Ag atoms.[19] PVP molecules preferentially adsorb onto specific crystallographic planes of silver, particularly the (100) and (111) facets, influencing the anisotropic growth and promoting nanowire formation over isotropic nanoparticle formation.[20] Additionally, PVP enhances adhesion between AgNWs and other carbon-based materials, including polymers, through multiple mechanisms.[21,22] The C=O groups in PVP act as anchors for hydrogen bonding, while the partially negative PVP–Ag NW complexes exhibit strong electrostatic interactions with protonated ES.[23] Moreover, PVP improves the dispersion of AgNWs in the reaction medium,[24] facilitating homogeneous subsequent deposition onto AgNWs, thereby enhancing their integration with PANI-based supercapacitor electrodes.

In this study, coaxial structures were fabricated, consisting of AgNWs as the core with two subsequent shells of carbon and PANI. The carbon layer is expected to bridge the highly conductive AgNWs and the semiconducting PANI, thereby creating an optimal platform for supercapacitors. Moreover, the mechanical flexibility of the individual components is expected to be retained in the resulting structures. The fabricated structures were systematically investigated with respect to their chemical composition and morphology. Furthermore, electrochemical measurements were performed to evaluate the specific capacitance and to elucidate the charge-storage characteristics.

Experimental

Materials

Silver nitrate ($AgNO_3$, 99%), poly(vinylpyrrolidone) (PVP, 95%), ferric chloride ($FeCl_3$, 99%), D-glucose (99%), ethylene glycol (99%), hydrochloric acid (HCl, 99%), sulfuric acid (H_2SO_4, 98%) and ammonium persulfate (APS, 99%) were obtained from Xilong. Aniline (C_6H_7N, 99%) was purchased from Sigma-Aldrich. Conductive carbon black (solid, 99%), polyvinylidene difluoride (PVDF, 99%) and *N*-methyl-2-pyrrolidone (NMP) were obtained from Fisher Scientific, and flexible indium tin oxide (ITO) coated PET (60 Ω sq^{-1}, 125 μm) was purchased from Sigma-Aldrich.

Synthesis of AgNWs

First, 0.163 g of PVP was added to 22 mL of ethylene glycol (EG), and the temperature of the mixture was increased to 140 °C. Prior to this, 2.5 mL of $FeCl_3$ solution with a concentration of 600 μM and 3 mL of an EG solution with a concentration of 1 mM were prepared in ethylene glycol. These solutions were then gradually added to the reaction mixture over 1 minute, and the mixture was continuously stirred for an additional 50 minutes. After the reaction, the mixture was allowed to cool to room temperature, centrifuged at 9500 rpm for 10 minutes, and thoroughly washed with distilled water and ethanol. Finally, the product was dispersed in 30 mL of ethylene glycol and stored at 4 °C for further use.

Synthesis of the coaxial AgNWs/PANI nanocomposite

7 g of glucose was first dispersed in the AgNW dispersion, and the mixture was heated to 180 °C with continuous stirring. The reaction was maintained for 60 minutes. This step was performed to obtain an amorphous carbon layer on the AgNWs. Then, the mixture was allowed to cool to room temperature, centrifuged, and washed with water and ethanol, denoted as C@AgNWs. The black C@AgNWs was then dispersed in 300 mL of HCl containing 92 μL of aniline. The mixture was then placed in an ice bath, maintained at temperatures between 0 and 5 °C. Subsequently, 0.2282 g of APS, diluted in 20 mL of HCl, was added to the mixture, and stirring was continued for 1 hour. The resulting mixture was then left undisturbed in a refrigerator at 4 °C for 24 hours, leading to the formation of a darkish blue-colored product. The product was washed several times with ethanol and dried at ambient temperature, denoted as PANI@C@AgNWs. For comparison, AgNWs were directly used for depositing the PANI layer, as described in the procedure above, without using amorphous carbon as an intermediate layer. The resulting product was denoted as PANI@AgNWs. Additionally, bulk PANI was prepared using the same polymerization procedure.

Characterization

X-ray diffraction (XRD, D8 Phaser, Bruker) was used to analyze the crystallographic structure of the as-prepared materials, utilizing a Cu-Kα radiation source with a wavelength of 0.154 nm. The morphological characteristics were examined using field-emission scanning electron microscopy (FE-SEM, Hitachi S-4800) and high-resolution transmission electron microscopy (HR-TEM, JEM-1010, Jeol) at 200 kV. X-ray photoelectron spectroscopy (XPS, PHI 5000 Versaprobe II) with an energy source of 187 eV was used to investigate the chemical composition and bonding states. Raman spectroscopy (XploRa Plus, 785 nm, Horiba) was conducted to analyze the structural vibrations within the materials.

Fabrication of working electrodes and electrochemical measurements

The as-prepared materials were used to fabricate working electrodes using the doctor-blade method. Specifically, the active materials, carbon black powder, and PVDF (pre-diluted in NMP at 80 mg mL^{-1}) were ground together at a mass ratio of 75 : 15 : 10. The resulting mixture was evenly coated onto a graphite/ITO substrate and then dried at 80 °C for 12 hours. The mass of active materials was determined to be approximately 0.45 mg per working electrode. The graphite substrate, now coated with active materials, was subsequently used for electrochemical measurements. For electrochemical impedance spectroscopy (EIS) and galvanostatic charge–discharge (GCD) measurements, the graphite substrate served as the working electrode (WE) in a Swagelok-type cell, tested using a Lanhe CT3001 battery testing system, as depicted in Fig. S1a and b. In this setup, two WEs were separated by a membrane soaked in 1 M H_2SO_4. For cyclic voltammetry (CV) measurements, a three-electrode

system (Gamry REF 600) was implemented, with the graphite substrate as the working electrode, a platinum rod as the counter electrode, and an Ag/AgCl electrode as the reference electrode, also using 1 M H_2SO_4 as the electrolyte (Fig. S1c).

The specific capacitance – SC (F g^{-1}) was calculated from GCD curves as follows:[25]

$$\mathrm{SC} = \frac{I \times \Delta t}{m \times \Delta V} \quad (1)$$

The SC was also determined from CV curves using the following equation:[26,27]

$$\mathrm{SC} = \frac{A}{2 \times m \times v \times \Delta V} \quad (2)$$

where I is the constant current (A), Δt is the discharge time (s), ΔV is the potential window (V), and m is the total weight of active materials deposited on the working electrode (WE) (g), A is the area enclosed by the CV curve, and v is the scan rate (V s^{-1}).

Results and discussion

The morphologies of the as-prepared materials are revealed in SEM images (Fig. 1), showing distinct differences. The AgNWs had diameters of approximately 51 ± 10 nm and a length of about 2.7 ± 0.6 μm, corresponding to an aspect ratio of 51 (length-to-diameter). Notably, the nanowires exhibited significant coherence in shape and morphology, appearing as cylindrical-like wires. Meanwhile, the C@AgNWs showed a significant reduction in length to approximately 1.1 ± 0.5 μm and an increase in diameter to 65 ± 17 nm. This can be attributed to the decomposition of glucose into carbon fragments at high temperatures, which subsequently anchored onto the AgNW surface, forming an amorphous carbon layer consisting of sp^2 and sp^3 carbon atoms.[28,29] During this process, the original AgNWs fragmented into shorter wires due to heat-induced stress, leading to concomitant irregularities in the size and shape of the C@AgNWs. Upon PANI deposition *via in situ* polymerization at low temperatures, the PANI@C@AgNWs exhibited a notable increase in diameter to 181 ± 57 nm, while the length remained approximately the same at 1.2 ± 0.6 μm. Importantly, nanostructured PANI was observed on the surface, completely covering the underlying C@AgNWs with PANI nanowires, and the thickness was estimated to be approximately 116 nm. It was evident that the original AgNWs were sequentially coated with amorphous carbon and PANI nanowires, forming coaxial wire-like structures. Additionally, PANI nanowires were directly deposited onto the AgNWs, resulting in the formation of PANI@AgNWs, which exhibited a similar coaxial structure. However, these structures appeared more uniform in size and shape compared to the more variable appearance of PANI@C@AgNWs, with diameters of 182 ± 43 nm and lengths of 1.9 ± 0.9 μm. This improved uniformity is attributed to the intrinsic consistency of the underlying AgNWs, as previously discussed. As a result, the AgNWs decorated with PVP demonstrated strong adhesion with carbon and PANI materials, which is expected to play a significant role in the electrochemical characteristics of the as-prepared materials. For comparison, bulk PANI, prepared using the same procedure without AgNWs, was also investigated (Fig. S2). The SEM images revealed large aggregates with non-uniform shapes, indicating that PANI nanowires form only when incorporated with substrate materials such as AgNWs and/or PANI@AgNWs.

Further investigation was conducted using XRD. As shown in Fig. 2, the XRD pattern of AgNWs displays all characteristic peaks located at 2θ = 38.5°, 45.1°, 65.4°, and 78.5°, corresponding to the (111), (200), (220), and (311) facets, respectively, indicating the formation of solid Ag.[30] These peaks persisted in the pattern of C@AgNWs, suggesting that the amorphous carbon coating formed at high temperatures did not alter the crystalline structure of the underlying AgNWs. Amorphous carbon generally does not exhibit XRD peaks due to its lack of long-range crystalline order.[31] Notably, the deposition of PANI was confirmed by the presence of peaks located at 2θ = 29° and 31°, corresponding to the (113) and (322) facets,[32] which are characteristic of the crystalline structure of PANI. All peaks corresponding to AgNWs were significantly diminished in intensity, which can be attributed to the complete coverage of crystalline PANI on the AgNWs, as discussed in the SEM analysis above.

The chemical states of the as-prepared materials were analyzed using XPS spectra (Fig. 3 for the XPS spectra of PANI@C@AgNWs and Fig. S3 for all the materials). Three core-level orbitals were examined: Ag 3d, C 1s, and N 1s. In the Ag 3d orbital, all four materials exhibited characteristic peaks, which were deconvoluted into smaller peaks at specific binding energies (BE) (as shown in Table 1), corresponding to Ag^0 and Ag_xO (primarily AgO and Ag_2O) present in solid Ag.[33,34] Notably, the intensities of these peaks gradually decreased in the order of AgNWs > C@AgNWs > PANI@C@AgNWs. This can be attributed to the subsequent deposition of materials onto the original AgNWs, which resulted in shielding and reducing the signal of the Ag 3d orbitals. This provides clear evidence that the core AgNWs remained intact after each subsequent deposition. Interestingly, the presence of PVP on AgNWs was confirmed, as the C 1s orbital of AgNWs exhibited peaks at BE = 296.7 eV and 287.9 eV, corresponding to C–N and C=O bonds in PVP molecules.[35] In the N 1s orbital, two distinct peaks for PANI were observed at BE = 400.5 eV and 402.5 eV, corresponding to benzenoid units and protonated amines,[36,37] respectively, confirming the presence of polyaniline. The C 1s orbital of C@AgNWs exhibited peaks corresponding to C–C/C–H bonds, similar to those in AgNWs. However, these peaks were more intense, indicating that the presence of the carbon layer increased the carbon density, rather than being solely attributed to PVP. Additionally, the peak at BE = 399.5 eV, assigned to the N–C bond in PVP,[38] was still present, further supporting the existence of PVP-stabilized AgNWs in the PANI@C@AgNWs structure. Together with the SEM and XRD results discussed above, the XPS analysis firmly demonstrates that the coaxial AgNWs–PANI structures were successfully fabricated. The structures of the amorphous carbon and PANI are revealed in the TEM images (Fig. 4). After deposition of the carbon layer,

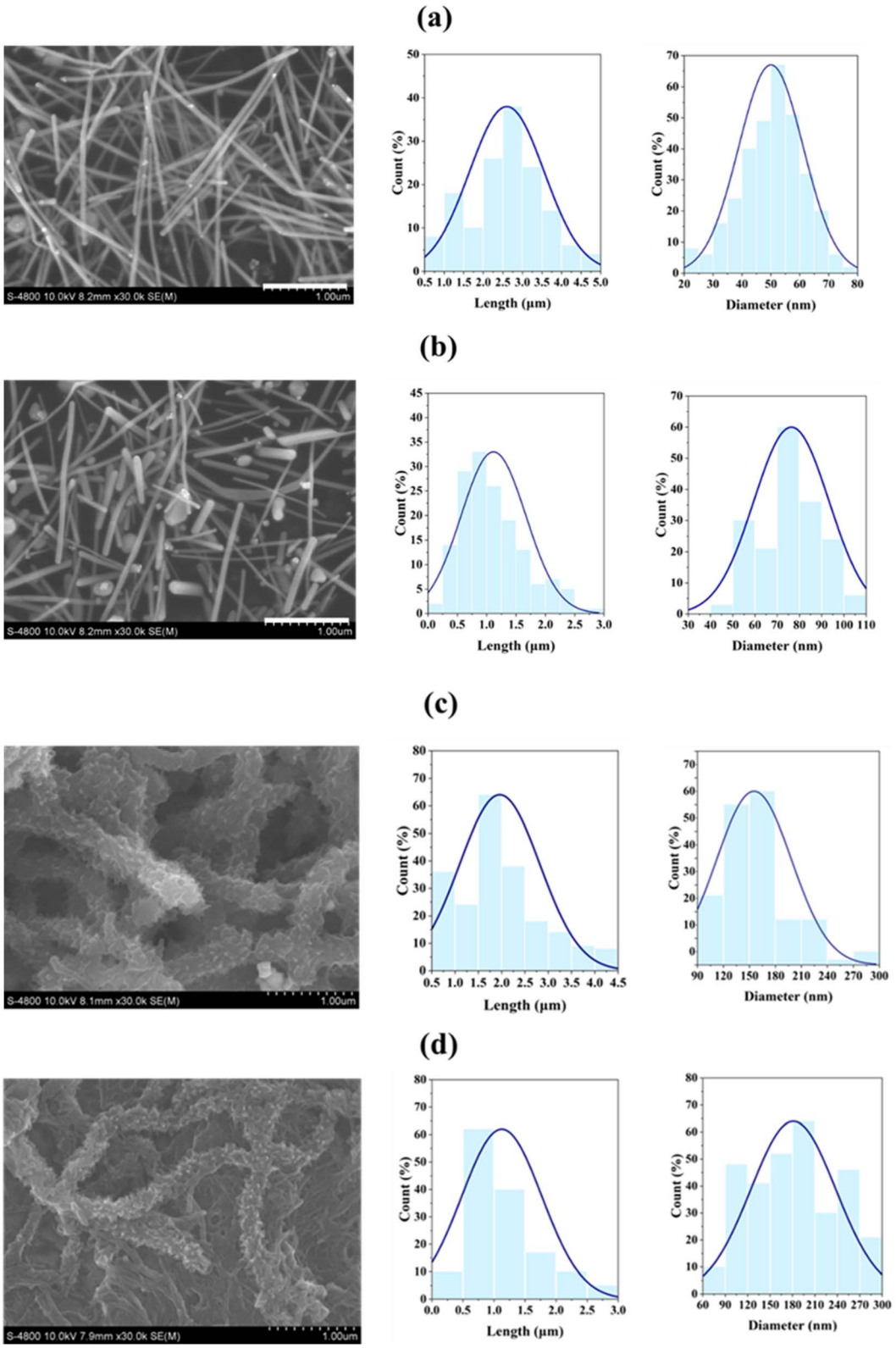

Fig. 1 SEM images and corresponding size distribution of (a) AgNWs, (b) C@AgNWs, (c) PANI@AgNWs, and (d) PANI@C@AgNWs.

the C@AgNWs exhibited a high degree of surface disorder, accompanied by a slight increase in diameter, indicating the formation of a thin carbon layer. In the case of PANI@C@AgNWs, a polymeric PANI coating was observed to wrap the C@AgNWs core, with a thickness ranging from 80 to 100 nm. This observation is in strong agreement with the SEM, XRD, and XPS results discussed above.

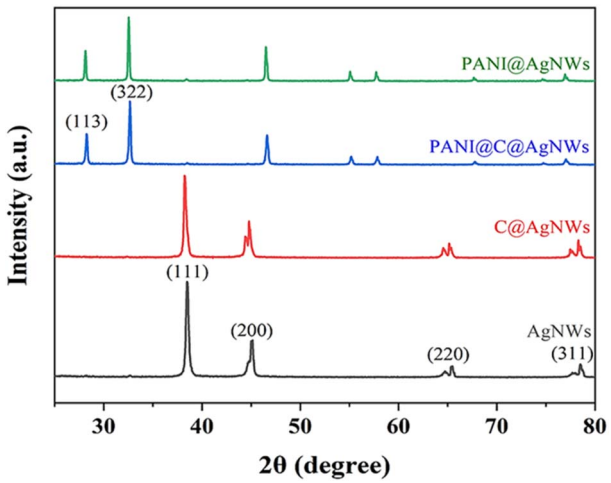

Fig. 2 XRD patterns of the as-prepared materials.

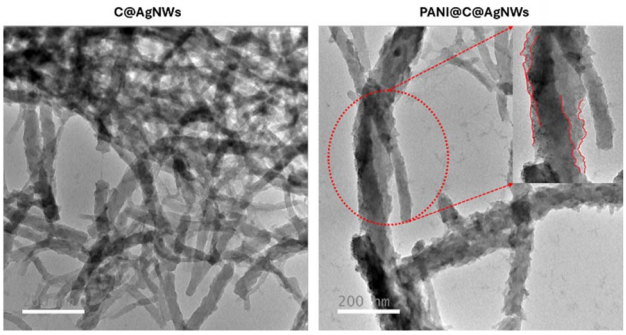

Fig. 3 XPS spectra of the as-prepared PANI@C@AgNWs, showing Ag 3d, C 1s, and N 1s orbitals.

Table 1 Binding energies corresponding to the Ag 3d orbitals present in the as-prepared materials

	Binding energy (eV)			
	Ag $3d_{5/2}$		Ag $3d_{3/2}$	
Sample	Ag^0	Ag_xO	Ag^0	Ag_xO
AgNWs	368.18	368.25	374.17	374.78
C@AgNWs	366.67	367.19	372.69	373.59
PANI@C@AgNWs	366.69	367.74	372.68	373.80
PANI@AgNWs	367.10	368.25	373.23	374.23

Further Raman measurements (Fig. 5) revealed that, in the C@AgNWs, carbon layers composed of sp^2-hybridized carbons were formed, as evidenced by the prominent G band at 1580 cm^{-1} and an increased G/D band intensity ratio compared to that of pristine AgNWs. In the case of PANI@C@AgNWs, characteristic vibrational peaks of PANI appeared in the region adjacent to the D band, including the $C–N^+$ stretching of the ES form, as well as the C–N stretching of the secondary aromatic amine at 1330 cm^{-1} and 1250 cm^{-1}, respectively.

To elucidate the influence of these layers on the electrical properties, EIS was performed to evaluate the charge transfer resistance (R_{ct}) from the Nyquist plots (Fig. 6). The R_{ct} values were determined to be 8.28 Ω, 3.73 Ω, and 1.43 Ω for PANI, PANI@AgNWs, and PANI@C@AgNWs, respectively. Clearly, the incorporation of AgNWs led to a significant enhancement in overall conductivity compared to pure PANI, which can be attributed to the intrinsically high electrical conductivity and excellent interfacial compatibility of AgNWs, as discussed previously. Notably, PANI@C@AgNWs exhibited a lower R_{ct} than PANI@AgNWs, highlighting the beneficial role of the carbon interlayer. As revealed by the Raman analysis, the carbon layer contained a substantial network of sp^2-hybridized carbons (layered sheets of sp^2 carbon atoms). Although the conductivity of this amorphous carbon was lower than that of pristine AgNWs, it served as an effective intermediate buffering layer between the highly conductive AgNWs and the semiconducting PANI. This hierarchical architecture facilitated a more efficient electrical conduction pathway. Similar interfacial modifying layers have been widely employed to reduce charge injection barriers in conductive composites.[39–41]

Among the investigated materials, PANI@C@AgNWs was expected to offer easier access for the intercalation and deintercalation of charges during charge–discharge cycles, facilitating faster redox reactions. Following this, the Swagelok model was still applied to conduct GCD measurements for the as-prepared materials. Fig. 7a shows the GCD curves for PANI@C@AgNWs at different current densities. At 0.5 A g^{-1}, an asymmetrical curve was observed, indicating resistive losses.[42,43] From 1 A g^{-1} to 4 A g^{-1}, nearly symmetrical charge and discharge curves were obtained, indicating high reversibility and good electrochemical stability. From these curves, the corresponding specific capacitance (SC) values were calculated to range from 261 F g^{-1} to 96 F g^{-1}, as shown in Fig. 7b. At low current densities, the discharge process occurs more gradually, allowing for more complete utilization of active materials, resulting in higher specific capacitance. This is derived from eqn (1), which shows that capacitance increases as the discharge time is longer for the same voltage range. Additionally, a current density of 10 A g^{-1} was applied to evaluate the fast-charging capability of the material (Fig. S4). Under this condition, the discharge time was only 2 s, and the SC was calculated to be 18 F g^{-1}. Therefore, a current density of 1 A g^{-1} was also chosen to investigate the GCD curves for PANI and PANI@AgNWs using a potential range from −0.3 to 0.8 V (Fig. 7c). These materials exhibited good symmetrical GCD curves. However, their discharge times were significantly quicker, corresponding to SC values of 99 F g^{-1} and 109 F g^{-1}, compared to 184 F g^{-1} obtained for PANI@C@AgNWs. Furthermore, 3000 charge–discharge cycles were conducted for all the materials (Fig. 7d). PANI@C@AgNWs exhibited the highest SC and experienced a capacitance loss of 47% compared to the initial value after 3000 cycles, whereas the losses for PANI@AgNWs and PANI were 51% and 89%, respectively. Remarkably, the XRD patterns of PANI@C@AgNWs after 3000 GCD cycles (Fig. S5) revealed that the chemical structure remained unchanged, with dominant peaks corresponding to

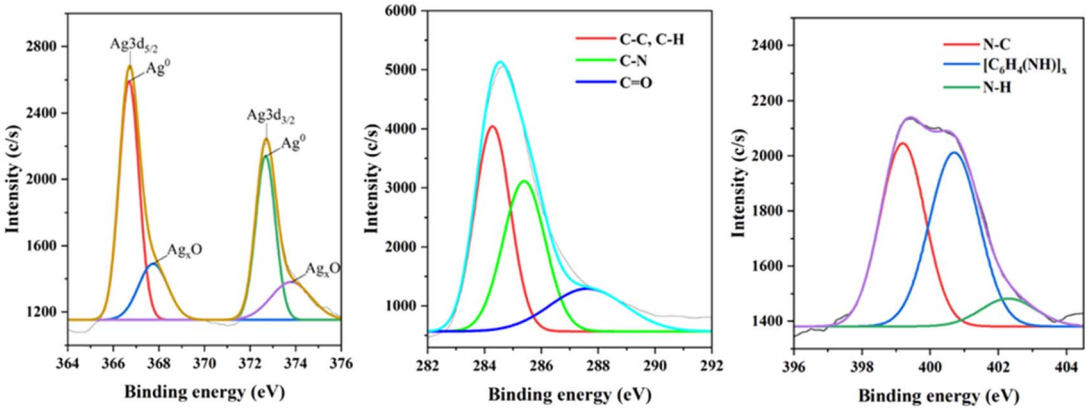

Fig. 4 TEM images of the as-prepared materials, the scale bar is 200 nm.

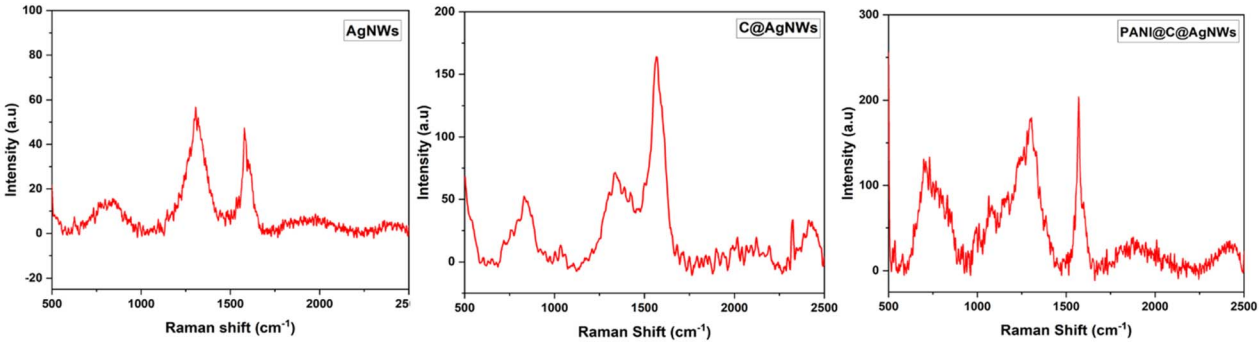

Fig. 5 Raman spectra of the as-prepared materials using an excitation wavelength of 785 nm.

conductive carbon ($2\theta = 25°$) and the (113) and (322) facets of PANI. This strongly indicates that the material exhibits excellent structural stability under working conditions.

Further investigation was conducted to elucidate the role of the carbon layer and the mechanism by which charges are stored. CV measurements were performed using a three-electrode system, and the results are shown in Fig. 8. First, different potential ranges were investigated at a scan rate of 40 mV s^{-1} (Fig. 8a). Within the potential range of −0.3 to 0.8 V, the oxidation and reduction processes of PANI@C@AgNWs were completed. The first anodic peak, located at 0.33 V, corresponds to the oxidation of leucoemeraldine salt (LS) to ES. The second anodic peak at 0.58 V is associated with the redox conversion between bipolarons and polarons, facilitated by the hydrolysis of PANI.[44,45] During the reverse scan (0.8 to −0.3 V), the corresponding reduction process occurs, forming cathodic peaks symmetrical to the anodic peaks, indicating the good reversibility of the PANI@C@AgNWs. To investigate the pseudocapacitive behavior of PANI@C@AgNWs, CV measurements were conducted at different scan rates (Fig. 8b). The corresponding SC was calculated using eqn (2). As shown in Fig. 8c, SC decreases with increasing scan rate. A relationship between the current density (i) and scan rate (v) was established according to the following equation:[46,47]

$$\log(i) = b\log(v) + c \quad (3)$$

where i is the current density (A g^{-1}) at different scan rates, v is the scan rate (mV s^{-1}), and b and c are constants. From the CV curves at different scan rates, the anodic and cathodic peak current densities were determined. As depicted in Fig. 8d, the b values were found to be 0.79 and 0.88 for the anodic and

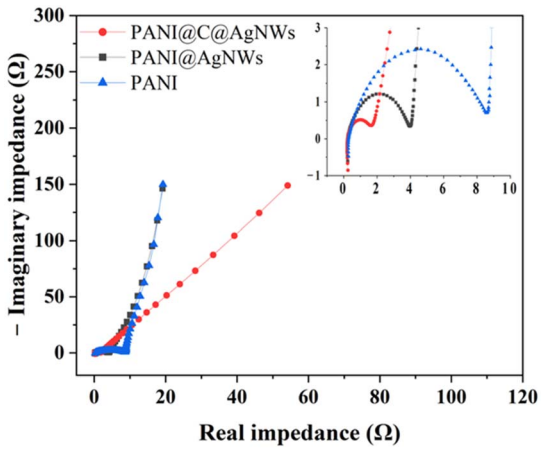

Fig. 6 Nyquist plots of the as-prepared materials measured using the Swagelok model. Measurements were conducted over a frequency range of 0.01 Hz to 1 MHz.

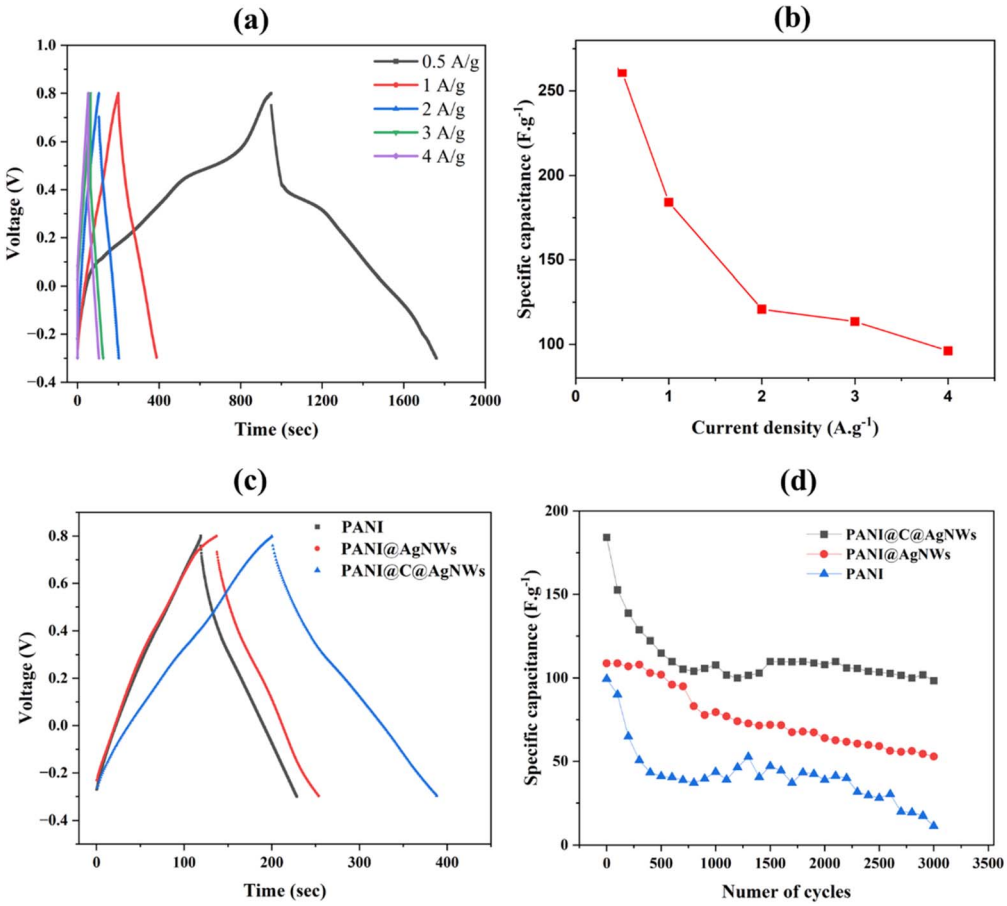

Fig. 7 (a) GCD curves of PANI@C@AgNWs obtained at different current densities, conducted over a potential range of −0.3 to 0.8 V, (b) specific capacitance values calculated at different current densities using the GCD curves, (c) GCD curves of PANI, PANI@AgNWs, and PANI@C@AgNWs, and (d) specific capacitance values recorded over 3000 charge–discharge cycles for the as-prepared materials.

cathodic peaks, respectively. This range of b values suggests that PANI@C@AgNWs store electrical charges through both EDLC(non-faradaic) and redox reactions (faradaic).[48] To further clarify the contributions of faradaic and non-faradaic charge storage, the Dunn method was applied using the following relationships:[49,50]

$$i(v) = k_1 v + k_2 \sqrt{v}, \quad (4)$$

and

$$\frac{i(v)}{\sqrt{v}} = k_1 \sqrt{v} + k_2, \quad (5)$$

where $i(v)$ is the current obtained from CV at scan rate v (mV s^{-1}). Fig. 8e and f depict the percentage of capacitance contributions calculated using the Dunn method at different scan rates. It is evident that charge storage primarily occurs through a non-faradaic mechanism, in which charges are stored physically at the electrode–electrolyte interface, forming an EDLC without involving chemical reactions. The percentage of non-faradaic processes increases with scan rate, ranging from 69% to 88% as the scan rate increases from 5 to 100 mV s^{-1}. Interestingly, PANI is generally known for its dominant pseudocapacitive behavior (faradaic).[3,5]

However, in PANI@C@AgNWs, EDLC (non-faradaic) is the dominant charge storage mechanism. At this stage, the role of the underlying carbon layer has been elucidated. The carbon materials primarily store charges through EDLC,[51,52] which eventually contributes to the overall capacitance of PANI@C@AgNWs. At high scan rates, EDLC percentage also increases accordingly, as non-faradaic processes are favored at high scan rates.[52] In contrast, faradaic processes, primarily redox reactions, tend to be more efficient at low to moderate scan rates, as chemical reactions require more time to complete.[53,54] The carbon layer has been demonstrated to play a crucial role in enhancing the capacitive behavior of PANI@C@AgNWs, not only by reducing R_{ct} for faster charge transport but also by dominating charge storage through EDLC.

Lastly, the as-prepared PANI@C@AgNWs was successfully transferred onto the flexible ITO-coated PET substrate (Fig. S1d), followed by GCD measurements. As shown in Fig. 9, at a current density of 0.5 A g^{-1}, the SC after 500 cycles was calculated to be 85 F g^{-1}. At a higher current density of 1 A g^{-1}, the SC gradually increased from ~10 F g^{-1} to nearly 40 F g^{-1} over 3000 cycles. This steady increase in capacitance suggests an extended electrochemical activation process, wherein the conductive network becomes progressively more efficient. Such

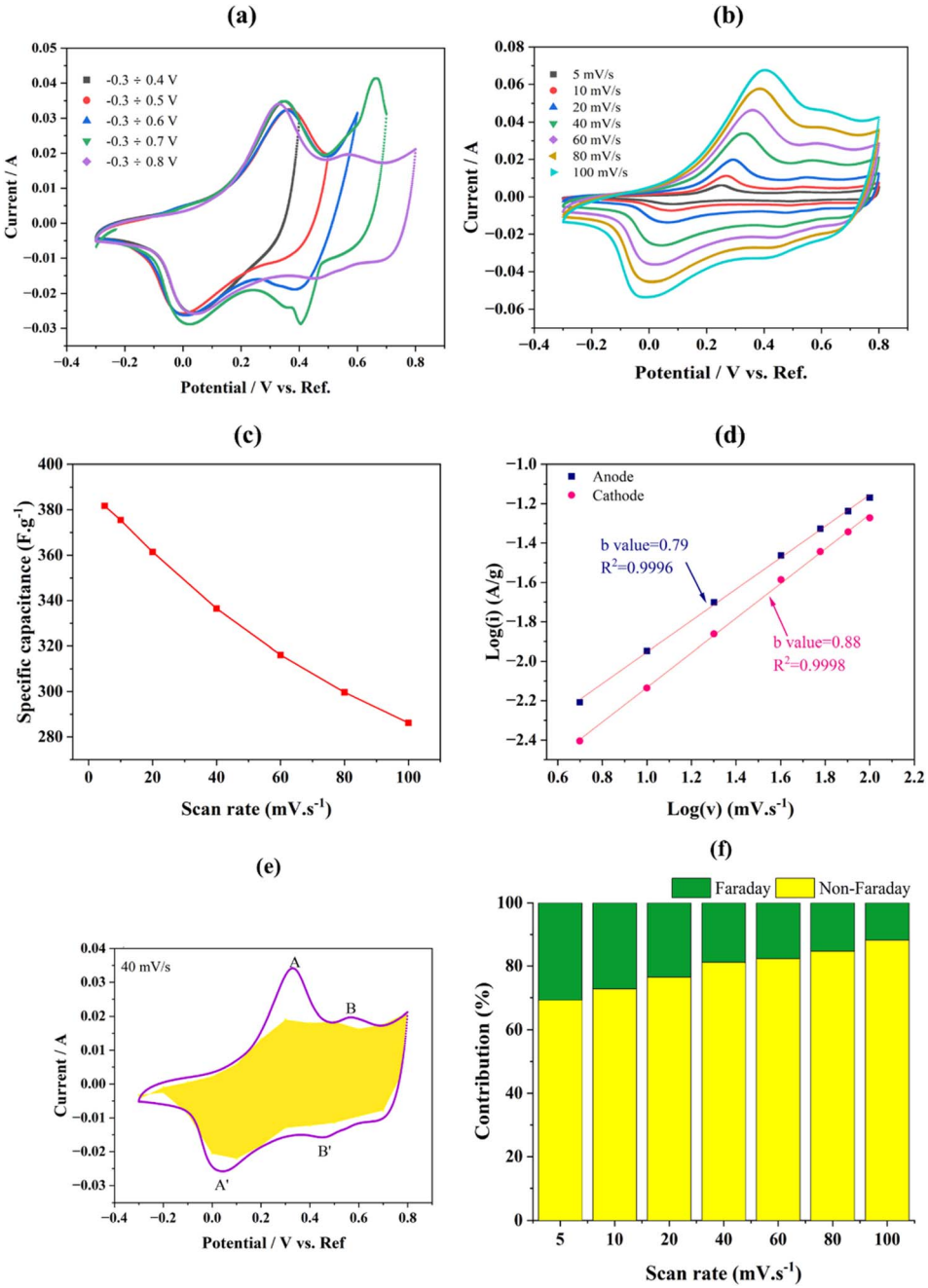

Fig. 8 Electrochemical characteristics of PANI@C@AgNWs: (a) CV curves at different potential ranges with a scan rate of 40 mV s^{-1}, (b) CV curves at different scan rates over a potential range of −0.3 to 0.8 V, (c) specific capacitance values calculated from the CV curves, (d) logarithmic relationship between the scan rate and current density, (e) CV curve showing the integrated area calculated using the Dunn method, (f) faradaic and non-faradaic capacitance contributions at different scan rates ranging from 5 to 100 mV s^{-1}.

self-conditioning behavior is characteristic of conducting polymers, particularly PANI, where repeated ion insertion and extraction promote chain rearrangements and enhance the accessibility of electroactive sites.[55,56] Although the SC values for PANI@C@AgNWs deposited on ITO-coated PET were lower than those obtained on graphite substrates, the ability to maintain electrochemical functionality on a flexible platform underscores the robustness and adaptability of the coaxial architecture. Importantly, these results highlight the practical feasibility of employing PANI@C@AgNWs in flexible supercapacitor devices, which are of great interest for next-generation portable and wearable electronics.

In comparison with prior studies, relative to representative PANI-based composites (Table 2), the SC of PANI@C@AgNWs at 1 A g^{-1} is comparable to that of α-Fe_2O_3 nanotube/PANI (185 F g^{-1} at 1 A g^{-1}) and falls within the range reported for rGO@-PANI–DBSA symmetric devices (134–173 F g^{-1} at 1 A g^{-1}), but remains below 3D cross-linked PANI (280.4 F g^{-1} at 1 A g^{-1}) and PANI nanowires on MOF-derived nanoporous carbon tested at a lower rate (534 F g^{-1} at 0.2 A g^{-1}). By contrast, semi-

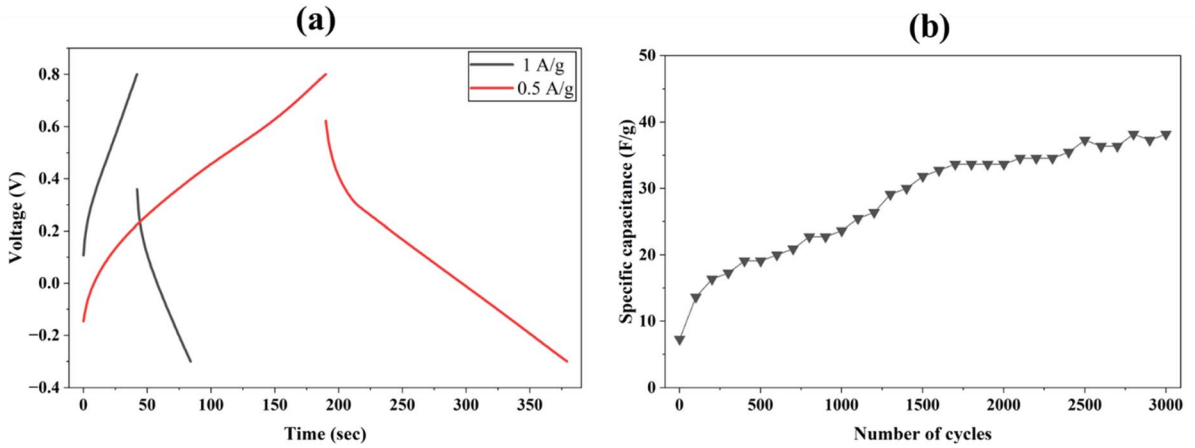

Fig. 9 (a) GCD curves of PANI@C@AgNWs deposited on ITO-coated PET at current densities of 0.5 and 1 A g^{-1}, (b) SC values of the as-prepared materials recorded over 3000 charge–discharge cycles at 1 A g^{-1}.

Table 2 Comparison of SC values obtained from GCD measurements with those reported in previous studies

Materials	Specific capacitance	Cyclic stability	Year	Ref.
3D cross-linked PANI network	280.4 F g^{-1} at 1 A g^{-1}	98% after 1000 cycles	2025	57
rGO@PANI–DBSA composites in 3D-printed symmetric devices	134–173 F g^{-1} at 1 A g^{-1}	77–85% after 5000 cycles	2024	58
α-Fe_2O_3 nanotube/PANI composite	185 F g^{-1} at 1 A g^{-1}	90.1% after 3000 cycles	2021	59
PANI nanowires on MOF-derived nanoporous carbon	534 F g^{-1} at 0.2 A g^{-1}	94.4% after 10 000 cycles	2021	60
Semi-polycrystalline PANI–activated carbon	45 F g^{-1} at 5 A g^{-1}	92.5% after 10 000 cycles	2023	61
PANI/SWNT thin film (transparent)	55 F g^{-1} at 5 A g^{-1}	n/a	2012	62
PANI@C@AgNWs (coaxial)	184 F g^{-1} at 1 A g^{-1}	53% after 3000 cycles	2025	This work

polycrystalline PANI–activated carbon shows markedly lower capacitance under high-rate operation (45 F g^{-1} at 5 A g^{-1}) despite excellent durability (92.5% retention over 10 000 cycles). Crucially, this work emphasizes the role of a thin amorphous carbon interlayer as an interfacial charge-transfer buffer at the AgNW/PANI junction, which reduces charge-transfer resistance and explains the observed rate performance and the predominance of EDLC at elevated scan rates. Such a mechanism has been insufficiently investigated in prior studies with PANI-based systems.

Conclusions

In this study, AgNWs were fabricated using PVP as a stabilizer, followed by the subsequent deposition of a carbon layer and PANI. The as-prepared materials were characterized by SEM, XRD, and XPS, confirming the formation of PANI nanowires on the outer layer of the core materials. The PANI@C@AgNWs structures exhibited an average diameter of 181 ± 57 nm and a length of 1.2 ± 0.6 μm, with PANI nanowires measuring approximately 116 nm in thickness. Furthermore, EIS revealed that the R_{ct} was 8.28 Ω, 3.73 Ω, and 1.43 Ω for PANI, PANI@AgNWs, and PANI@C@AgNWs, respectively, indicating a significant reduction in resistance with the incorporation of AgNWs and the carbon layer. The SC obtained from GCD measurements was 99 F g^{-1}, 109 F g^{-1}, and 184 F g^{-1} for PANI, PANI@AgNWs, and PANI@C@AgNWs, respectively. After 3000 charge–discharge cycles, the capacitance loss for PANI@C@AgNWs was 47%, compared to 51% for PANI@AgNWs and 89% for PANI, demonstrating improved cycling stability. The presence of the intermediate carbon layer was found to be crucial for enhancing charge transfer and contributing significantly to overall capacitance *via* EDLC.

Author contributions

Pham Thi Thuy Nga: conceptualization, methodology, investigation, writing; Nguyen Van Quy: data curation; Dinh Khoi Dang: sample preparation; Nguyen Thanh Sang: software; Ho Phuong: technical support; Nguyen Tran Nhac Khoa: resources; To Minh Dai: technical support; Huynh Le Thanh Nguyen: conceptualization, supervision, writing – review & editing; Ly Tan Nhiem: conceptualization, methodology, supervision, writing – review & editing.

Conflicts of interest

There are no conflicts to declare.

Data availability

The data supporting this article have been included as part of the SI. Supplementary information is available. See DOI: **https://doi.org/10.1039/d5na00402k**.

References

1 A. H. Majeed, L. A. Mohammed, O. G. Hammoodi, S. Sehgal, M. A. Alheety, K. K. Saxena, S. A. Dadoosh, I. K. Mohammed, M. M. Jasim and N. U. Salmaan, *Int. J. Polym. Sci.*, 2022, **2022**, 9047554.

2 J. Banerjee, K. Dutta, M. A. Kader and S. K. Nayak, *Polym. Adv. Technol.*, 2019, **30**, 1902–1921.

3 S. Grover, S. Goel, R. B. Marichi, V. Sahu, G. Singh and R. K. Sharma, *Electrochim. Acta*, 2016, **196**, 131–139.

4 B.-X. Zou, Y. Liang, X.-X. Liu, D. Diamond and K.-T. Lau, *J. Power Sources*, 2011, **196**, 4842–4848.

5 A. V. Sosunov, M. Rajapakse, G. A. Rudakov, R. S. Ponomarev, V. K. Henner, J. B. Jasinski, D. A. Buchberger, M. S. Reza, B. Karki and G. Sumanasekera, *Surf. Engin. Appl. Electrochem.*, 2022, **58**, 87–93.

6 W. Chen, R. B. Rakhi and H. N. Alshareef, *J. Phys. Chem. C*, 2013, **117**, 15009–15019.

7 X. Chu, W. Yang and H. Li, *Mater. Horiz.*, 2023, **10**, 670–697.

8 N. Choudhary, A. Tomar, S. Bhardwaj, J. Ćwiertnia, D. Just, D. Janas, R. Chandra and P. K. Maji, *J. Mater. Chem. A*, 2025, **13**, 4012–4042.

9 W. Liu, C. Lu, H. Li, R. Y. Tay, L. Sun, X. Wang, W. L. Chow, X. Wang, B. K. Tay, Z. Chen, J. Yan, K. Feng, G. Lui, R. Tjandra, L. Rasenthiram, G. Chiu and A. Yu, *J. Mater. Chem. A*, 2016, **4**, 3754–3764.

10 Z. J. Han, C. Huang, S. S. Meysami, D. Piche, D. H. Seo, S. Pineda, A. T. Murdock, P. S. Bruce, P. S. Grant and N. Grobert, *Carbon*, 2018, **126**, 305–312.

11 S. S. Shah, S. Oladepo, M. A. Ehsan, W. Iali, A. Alenaizan, M. N. Siddiqui, M. Oyama, A.-R. Al-Betar and M. A. Aziz, *Chem. Rec.*, 2024, **24**, e202300105.

12 M. A. A. Shanmuganathan, A. Raghavan and S. Ghosh, *Phys. Chem. Chem. Phys.*, 2023, **25**, 7611–7628.

13 Y. Sun, *Nanoscale*, 2010, **2**, 1626–1642.

14 N. Hang, N. H. Hieu and L. T. Nhiem, *J. Mater. Sci.: Mater. Electron.*, 2023, **34**, 90.

15 L. Zhang, T. Song, L. Shi, N. Wen, Z. Wu, C. Sun, D. Jiang and Z. Guo, *J. Nanostruct. Chem.*, 2021, **11**, 323–341.

16 F. Basarir, Z. Madani and J. Vapaavuori, *Adv. Mater. Interfaces*, 2022, **9**, 2200866.

17 C. Zhao, B. Deng, G. Chen, B. Lei, H. Hua, H. Peng and Z. Yan, *Nano Res.*, 2016, **9**, 963–973.

18 D. P. Langley, G. Giusti, M. Lagrange, R. Collins, C. Jiménez, Y. Bréchet and D. Bellet, *Sol. Energy Mater. Sol. Cells*, 2014, **125**, 318–324.

19 L. Zhang and G. Feng, *Nanoscale*, 2020, **12**, 10573–10583.

20 P. Zhang, I. Wyman, J. Hu, S. Lin, Z. Zhong, Y. Tu, Z. Huang and Y. Wei, *Mater. Sci. Eng., B*, 2017, **223**, 1–23.

21 Y.-J. Song, M. Wang, X.-Y. Zhang, J.-Y. Wu and T. Zhang, *Nanoscale Res. Lett.*, 2014, **9**, 17.

22 K. S. Lau, S. X. Chin, S. T. Tan, F. S. Lim, W. S. Chang, C. C. Yap, M. H. H. Jumali, S. Zakaria, S. W. Chook and C. H. Chia, *J. Alloys Compd.*, 2019, **803**, 165–171.

23 K. Afshinnia, M. Sikder, B. Cai and M. Baalousha, *J. Colloid Interface Sci.*, 2017, **487**, 192–200.

24 M. Han, Y. Ge, J. Liu, Z. Cao, M. Li, X. Duan and J. Hu, *J. Mater. Chem. A*, 2020, **8**, 21062–21069.

25 S. T. Senthilkumar, R. K. Selvan, Y. S. Lee and J. S. Melo, *J. Mater. Chem. A*, 2012, **1**, 1086–1095.

26 X. Pu, D. Zhao, C. Fu, Z. Chen, S. Cao, C. Wang and Y. Cao, *Angew. Chem., Int. Ed.*, 2021, **60**, 21310–21318.

27 O. Gharbi, M. T. T. Tran, B. Tribollet, M. Turmine and V. Vivier, *Electrochim. Acta*, 2020, **343**, 136109.

28 S. Suganuma, K. Nakajima, M. Kitano, D. Yamaguchi, H. Kato, S. Hayashi and M. Hara, *J. Am. Chem. Soc.*, 2008, **130**, 12787–12793.

29 R. S. Assary and L. A. Curtiss, *Energy Fuels*, 2012, **26**, 1344–1352.

30 D. Kumar, Kavita, K. Singh, V. Verma and H. S. Bhatti, *Appl. Nanosci.*, 2015, **5**, 881–890.

31 P. K. Chu and L. Li, *Mater. Chem. Phys.*, 2006, **96**, 253–277.

32 M. Ayad, G. El-Hefnawy and S. Zaghlol, *Chem. Eng. J.*, 2013, **217**, 460–465.

33 K. Sharma, R. Singh, S. Sharma, C. S. P. Tripathi and D. Guin, *Colloids Surf., A*, 2024, **686**, 133332.

34 P. Kumari and P. Majewski, *J. Nanomater.*, 2013, **2013**, 839016.

35 F. Zhang, C. Yang, X.-X. Wang, R. Li, Z. Wan, X. Wang, Y. Wan, Y.-Z. Long and Z. Cai, *Appl. Sci.*, 2020, **10**, 596.

36 M. M. Mahat, D. Mawad, G. W. Nelson, S. Fearn, R. G. Palgrave, D. J. Payne and M. M. Stevens, *J. Mater. Chem. C*, 2015, **3**, 7180–7186.

37 Y. Xie and Y. Chen, *J. Mater. Sci.*, 2021, **56**, 10135–10153.

38 W. N. A. Aziz, A. Bumajdad, F. Al Sagheer and M. Madkour, *Mater. Chem. Phys.*, 2020, **249**, 122927.

39 S. H. Sung, N. Bajaj, J. F. Rhoads, G. T. Chiu and B. W. Boudouris, *Org. Electron.*, 2016, **37**, 148–154.

40 S. K. Mathialagan, S. O. Parreiras, M. Tenorio, L. Černa, D. Moreno, B. Muñiz-Cano, C. Navío, M. Valvidares, M. A. Valbuena, J. I. Urgel, P. Gargiani, R. Miranda, J. Camarero, J. I. Martínez, J. M. Gallego and D. Écija, *Adv. Sci.*, 2024, **11**, 2308125.

41 S. H. Jin, J. S. Yu, J. W. Kim, C. A. Lee, B.-G. Park, J. D. Lee and J. H. Lee, *SID Symposium Digest of Technical Papers*, 2003, vol. 34, pp. 1088–1091.

42 Y. Zhang, X. Li, Z. Li and F. Yang, *J. Energy Storage*, 2024, **86**, 111122.

43 F. Licht, M. A. Davis and H. A. Andreas, *J. Power Sources*, 2020, **446**, 227354.

44 Y. Lee, C. Chang, S. Yau, L. Fan, Y. Yang, L. O. Yang and K. Itaya, *J. Am. Chem. Soc.*, 2009, **131**, 6468–6474.

45 Q. B. Le, T.-H. Nguyen, H. Fei, C. Bubulinca, L. Munster, N. Bugarova, M. Micusik, R. Kiefer, T. T. Dao, M. Omastova, N. E. Kazantseva and P. Saha, *Sci. Rep.*, 2022, **12**, 664.

46 W. Xu, C. Sun, K. Zhao, X. Cheng, S. Rawal, Y. Xu and Y. Wang, *Energy Storage Mater.*, 2019, **16**, 527–534.

47 G. Qiu, Y. Guo, Y. Zhang, X. Zhao, J. Xu, S. Guo, F. Guo and J. Wu, *Ind. Eng. Chem. Res.*, 2022, **61**, 16034–16049.

48 R. M. Ghanem, D. A. Kospa, A. I. Ahmed, A. A. Ibrahim and A. Gebreil, *RSC Adv.*, 2023, **13**, 29252–29269.

49 Y. Wang, Y. Song and Y. Xia, *Chem. Soc. Rev.*, 2016, **45**, 5925–5950.
50 T. Brezesinski, J. Wang, S. H. Tolbert and B. Dunn, *Nat. Mater.*, 2010, **9**, 146–151.
51 M. G. Ashritha and K. Hareesh, in *Smart Supercapacitors*, ed. C. M. Hussain and M. B. Ahamed, Elsevier, 2023, pp. 179–198.
52 E. Frackowiak and F. Béguin, *Carbon*, 2001, **39**, 937–950.
53 R. Huang and Y. Xie, *J. Alloys Compd.*, 2024, **1002**, 175367.
54 S. Karthikeyan, B. Narenthiran, A. Sivanantham, L. D. Bhatlu and T. Maridurai, *Mater. Today: Proc.*, 2021, **46**, 3984–3988.
55 G. Yang, T. Takei, S. Yanagida and N. Kumada, *Molecules*, 2019, **24**, 976.
56 Y. Xie and X. Sha, *Synth. Met.*, 2018, **237**, 29–39.
57 Y. Yeszhan, S. Duisenbekov, D. Kurmangaliyeva, D. Kazhigitova, P. Askar, Y. Tileuberdi, A. Konarov, S. Adilov and N. Nuraje, *RSC Adv.*, 2025, **15**, 1205–1211.
58 D. Scarpa, M. Iuliano, C. Cirillo, P. Iovane, C. Borriello, S. Portofino, E. Ponticorvo, S. Galvagno and M. Sarno, *Sci. Rep.*, 2024, **14**, 14998.
59 F. Azimov, J. Kim, S. M. Choi and H. M. Jung, *Nanomaterials*, 2021, **11**, 1557.
60 M. Yao, X. Zhao, Q. Zhang, Y. Zhang and Y. Wang, *Electrochim. Acta*, 2021, **390**, 138804.
61 N. Mahato, T. V. M. Sreekanth, K. Yoo and J. Kim, *Molecules*, 2023, **28**, 1520.
62 J. Ge, G. Cheng and L. Chen, *Nanoscale*, 2011, **3**, 3084–3088.